J. Fluid Mech. (1993), *vol.* 254, *pp.* 283–311

Buoyancy-induced flow in porous media generated near a drilled oil well. Part 1. The accumulation of filtrate at a horizontal impermeable boundary

By E. B. DUSSAN V. AND FRANCOIS M. AUZERAIS
Schlumberger-Doll Research, Old Quarry Road, Ridgefield, CT 06877-4108, USA

(Received 23 July 1992 and in revised form 8 February 1993)

A substantial amount of drilling fluid can invade a permeable bed during the drilling of an oil well. The presence of this fluid, often referred to as filtrate, can greatly influence the performance of instruments lowered into the wellbore for the purpose of locating these permeable beds. The invaded filtrate can also substantially alter the physical properties of the porous rock. For these reasons, it is of great interest to known where the filtrate goes upon entering the bed. The objective of this study is to quantify the influence of the difference in density between the filtrate and the naturally occurring formation fluid on the shape of the filtrate front as the filtrate invades the formation. This type of phenomenon is often referred to as buoyancy or gravity segregation. In this study, Part 1, we determine the behaviour of the filtrate as it accumulates (and spreads out) at a horizontal impermeable barrier within the formation. This is a combined theoretical and experimental study in which an X-ray CT scanner is extensively used to determine the appropriateness and limitations of the simplifying assumptions used in the theory. In Part 2, the flow of the invading filtrate within the entire bed will be presented. The problem addressed in Part 1 may be viewed from the broader, more fundamental, perspective, as a well-defined model fluid mechanics problem for flow in porous media. One fundamental issue infrequently addressed concerns the consequence on the dynamics of the fluids of heterogeneities, always present to some degree, in consolidated porous solids. The X-ray CT scanner enables the assessment of the appropriateness of modelling such porous solids as spatially homogeneous, a very popular assumption. This study also addresses the limitation of the small-slope approximation when a fluid–fluid interface occurs in a porous solid, an approximation which has enjoyed great success in free-surface fluid mechanics problems when no porous media is present.

1. Introduction

As soon as a drill bit starts penetrating a permeable zone, filtrate from the wellbore begins entering the formation. This is a direct consequence of safety consideration which require the pressure of the drilling fluid in the wellbore to be maintained at a much higher value than the pressure of the fluid within the porous rock, thus preventing a well from producing when it is in the process of being drilled. Massive invasion of drilling fluid is prevented by the immediate buildup of mud cake along the wellbore wall. Since the presence of the filtrate within the formation affects the performance and interpretation of instruments lowered into the wellbore for detecting the presence of hydrocarbons (commonly referred to as *logging tools*), knowledge of the location of the filtrate is highly desirable (Allen *et al.* 1991). The objective of this

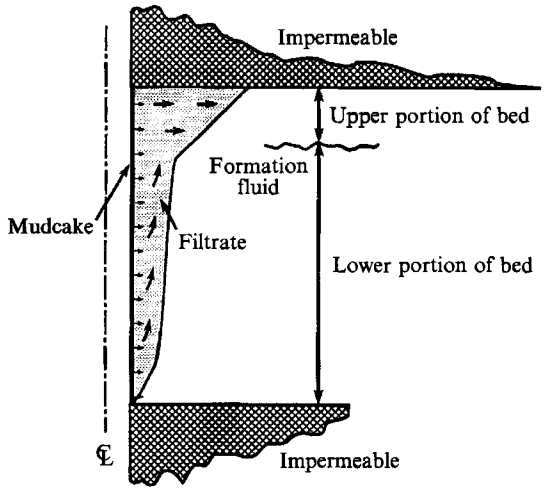

FIGURE 1. Illustration of Doll's results of the invasion of fresh filtrate into a salt-water-bearing sand formation bounded above and below by an impermeable matrix.

study is to quantify the movement of the filtrate arising from density differences between the filtrate and the formation fluid. This induced motion is often referred to as gravity segregation.

Henri Doll (1955) was the first to investigate the influence of gravity on the shape of the filtrate front (the interface formed between the filtrate and the formation fluid). His motivation was to find an explanation for very shallow invasion occurring in highly permeable beds. This contradicted the commonly held notion that shallow invasion only happened in beds having low permeability. His investigation, both theoretical and experimental, consisted of fresh water filtrate entering a bed fully saturated with salt water, from a vertical wellbore. He was able to demonstrate that buoyancy can cause the fresh filtrate to rise with an almost vertical trajectory at the wellbore wall, resulting in a rather shallow depth of invasion over the lower portion of the bed, and to accumulate beneath the upper impermeable bed boundary, resulting in deep invasion over the upper portion of the bed (see figure 1). Since his analysis was restricted to the lower portion of the bed, he was unable to estimate the dimensions (both the thickness and lateral extent) of the accumulated layer of filtrate beneath the upper impermeable bed boundary under field conditions. Knowledge of the dependence of the dimensions of this layer on the properties of the formation may aid in the determination of these properties from the analysis of log data.

Doll's study established the importance of two characteristic speeds: the radial speed at which the filtrate is forced to flow into the formation, and the vertical speed induced by the difference in density between the filtrate and the formation fluid. The ratio of these two speeds quantifies the importance of buoyancy, i.e. when the vertically induced speed 'greatly exceeds' the radially imposed speed then buoyancy effects are large. His combined experimental and theoretical results indicate that when buoyancy is large, the filtrate can be divided into two regions: a *vertical* layer contiguous with the wellbore wall occupying the lower portion of the bed in his study, and a *horizontal* layer consisting of filtrate spreading out across an impermeable horizontal barrier located in the upper region of his experiment. Thus our investigation concerns the dynamics of the horizontal layer in the large-buoyancy case.

This is Part 1 of a study of the invasion process. Here, the dynamic behaviour of the filtrate in the horizontal layer is quantified, i.e. the thickness and the depth of

penetration into the formation of accumulated filtrate at horizontal impermeable barriers are determined. The specific model introduced by Doll is adopted, that of a single horizontal bed through which is cut a vertical wellbore. Since our interest is over the timescale between the drilling of the permeable zone and the logging operation, we, like Doll, assume the wellbore instantaneously appears in the bed at time $t = 0$, having a mud cake in equilibrium with the dynamic conditions in the well. This is consistent with the current belief that as much as 95% of the volume of filtrate which has invaded the formation by the time the well is logged occurs under dynamic conditions in the presence of a mud cake (Gray & Darley 1980). That is to say, the volume of filtrate which invades the bed beneath the drill bit, and before the mud cake develops (spurt loss), or when static conditions prevail in the well (addition of new pipe sections to the drill string or drill bit replacement) is relatively small (references cited in Gray & Darley). Part 2 of this study (Dussan V. & Auzerais 1993) addresses the dynamics of the filtrate over the entire bed by combining these results with those of Doll.

A summary of the contents of this paper, Part 1, is as follows. Since this investigation depends upon Doll's, we begin in §2 with a brief presentation of his results. They are used to determine the rate at which filtrate is delivered to the horizontal layer. This represents our starting point. In §3, the equations and boundary conditions governing the dynamics of the filtrate and the formation fluid within the upper portion of the bed are simplified, consistent with the assumption of large buoyancy. Since our concern is with the dynamics of the fluid in the horizontal layer, the filtrate entering the layer is modelled as coming from a point source located on the impermeable boundary. This represents a self-contained well-defined model fluid mechanics problem of flow in porous media in which a moving 'free-surface' is present. We next identify the relevant scales for the vertical and radial spatial coordinates and velocity components, which are not obvious. A boundary-value problem is derived as the lowest-order problem resulting from a formal asymptotic expansion in terms of a parameter (a measure of the buoyancy strength). The same boundary-value problem was identified and solved by Barenblatt (see Barenblatt, Entov & Ryzhik 1990) who was interested in a different though related problem (refer to their chapter 3). (Barenblatt's work was initially published in Russian in the early 1950s.) The section ends with a presentation highlighting the method of solution, including the results relevant to this study. Experiments were performed to determine the appropriateness of the simplifying assumptions of our model, as well as the limitations introduced by only using the lowest-order term in an asymptotic expansion of the location of the filtrate front. Unlike Doll, who was restricted in his experiments to unconsolidated glass beads so that the motion of the dyed filtrate could be followed visually, we used an opaque commercial filter consisting of resin-cemented glass beads whose structure has similarities to porous rock (our future intent is to use porous rock). This was possible because the location of the filtrate, as it accumulated at the impermeable horizontal boundary, was followed using images taken with an X-ray CT scanner. The instrumentation, characterization of materials (porous solid, filtrate and formation fluids), experimental procedure, technique for extracting the location of the filtrate front from the images (pattern recognition) and results are all presented in §4. In §5, the results of the theory and experiment are discussed.

2. Vertical layer

We begin by discussing the dynamics of the filtrate contiguous to the wellbore, within what we have referred to as the vertical layer. This encompasses a presentation

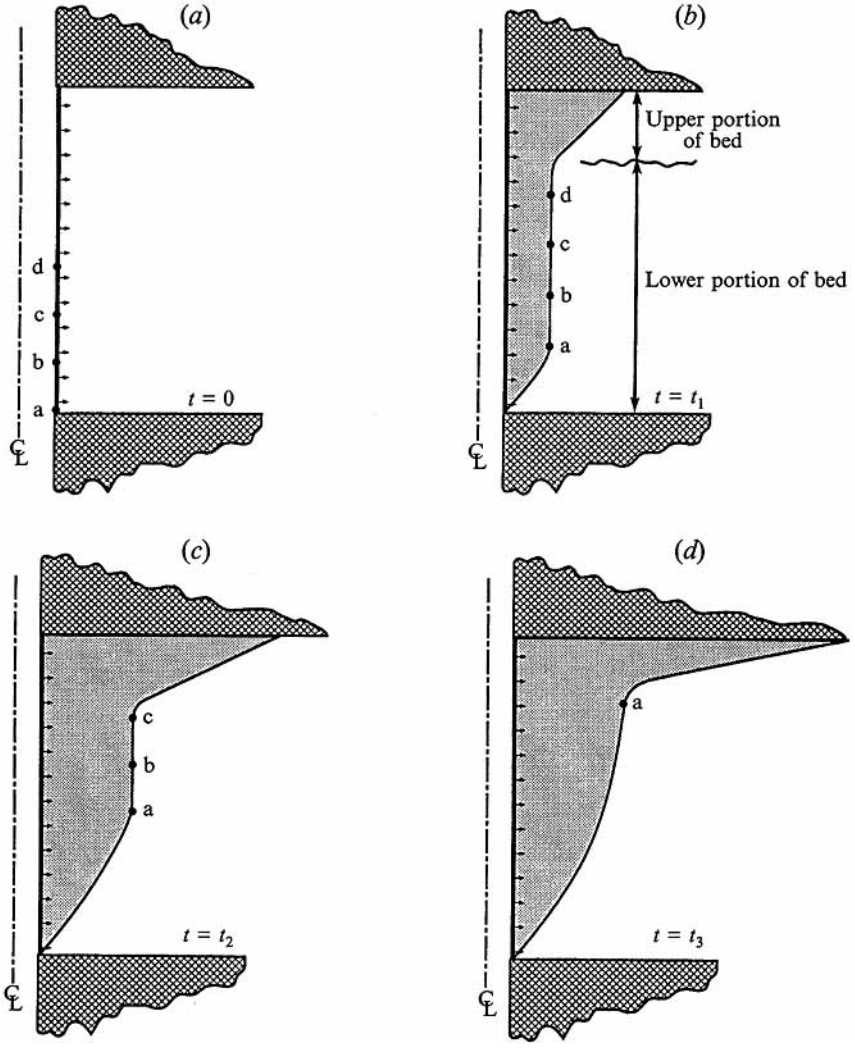

FIGURE 2. The development of the filtrate front as the filtrate invades the formation. In (*a*), four filtrate material points a–d located at the wellbore wall at time $t = 0$ are identified. Their subsequent positions within the lower portion of the bed are identified at three successive times $0 < t_1 < t_2 < t_3$ in (*b*), (*c*) and (*d*), respectively. By time t_3, the filtrate points b, c and d have entered the upper portion of the bed, with point a about to enter. In this illustration, $T = t_3$.

of the velocity field of the filtrate as it invades the formation and the time-dependent location of the filtrate front. Our objective is the identification of the rate at which filtrate enters the horizontal layer, a quantity needed in our investigation.

The following results are due to Doll (1955). He showed through simple reasoning, that when buoyancy dominates, the velocity of the filtrate, $\boldsymbol{u}_{ftl}$, within the formation is given by

$$\boldsymbol{u}_{ftl} = \frac{u_f R_{wb}}{r}\hat{\boldsymbol{r}} + W\hat{\boldsymbol{z}}, \tag{1}$$

where u_f denotes the (Darcy) speed of the filtrate as it enters the formation *at* the wellbore wall (not to be confused with u_{ftl} which shall denote $\boldsymbol{u}_{ftl} \cdot \hat{\boldsymbol{r}}$, the radial

component of the filtrate velocity evaluated at any point within the formation occupied by filtrate), R_{wb} denotes the wellbore radius, and $\hat{r}$ and $\hat{z}$ denote, respectively, local unit vectors in the radial and axial directions of a cylindrical coordinate system (r, θ, z) whose z-axis coincides with the centre of the wellbore and points upward (the plane $z = 0$ indicating the location of the lower impermeable boundary of the bed). The constant, W, appearing in (1) denotes $(\rho_{fil} - \rho_{for}) g k_v / \mu_{fil}$, where ρ and μ denote, respectively, the density and the viscosity of the fluid (the subscripts *fil* and *for* referring to the filtrate and the formation fluid, respectively), g denotes the gravitational constant (980 cm/s^2) and k_v denotes the vertical component of the permeability of the formation. (Sedimentary rocks, where oil is found, are known for being anisotropic. The vertical component of the permeability is smaller than the components in either horizontal direction, which are usually approximated to be equal.) The form of the filtrate velocity (1) is quite simple. Its radial component is identical to that of an incompressible fluid, having the same density as the formation fluid, entering the formation at constant speed u_f along the entire wellbore wall. The vertical component of (1) is an absolute constant, W, not varying with position within the formation nor over time. Thus the parameter $(\rho_{fil} - \rho_{for}) g k_v / \mu_{fil} u_f$ may be regarded as quantifying the influence of buoyancy. Equation (1) is based upon the assumption that almost all the pressure drop between the drilling fluid within the wellbore and the formation (not uncommon to be several hundred p.s.i.) occurs across the mud cake, a thin layer situated at the wellbore wall. A direct consequence is that the value of u_f is determined by the properties of the mud cake, not by the permeability of the formation. This is appropriate, under field conditions, for formations with horizontal component of permeability greater than approximately 10 mD.

Doll also determined the progression of the filtrate front. These results can be reconstructed by following the motion of a few material points as they enter the formation at time $t = 0$, refer to figure 2. The filtrate velocity (1) can be used to local these points at, say, four successive time $0 > t_1 > t_2 > t_3$. At each time, all of the points have advanced into the formation by the same distance, maintaining identical radial positions, and have risen vertically by the same amount, retaining their same vertical spacing until they have entered the horizontal layer. The curved section of the filtrate front, which begins to develop along its lower end, denotes the location of filtrate material points having entered the formation at position $(r, z) = (R_{wb}, 0)$ at times later than $t = 0$ (the θ-coordinate has not been specified due to azimuthal symmetry). The vertical straight section denotes the location of filtrate points at the wellbore wall at $t = 0$, possessing the same sort of trajectories as the material points discussed above. At time $\phi H_{for}/W$, denoted by T, the shape of the filtrate front has reached its steady-state configuration. This corresponds to the approximate time it takes the filtrate material point located at $(R_{wb}, 0)$ at time $t = 0$ to travel to the upper portion of the bed. The location of the filtrate front is summarized by

$$r = \begin{cases} (R_{wb}^2 + 2R_{wb} u_f z/W)^{\frac{1}{2}} & \text{for} \quad 0 < z < (t/T) H_{for} \\ (R_{wb}^2 + 2R_{wb} u_f t/\phi)^{\frac{1}{2}} & \text{for} \quad (t/T) H_{for} < z < H_{for} \end{cases} \quad \text{for} \quad t \leqslant T$$
$$(R_{wb}^2 + 2R_{wb} u_f z/W)^{\frac{1}{2}} \quad \text{for} \quad 0 < z < H_{for} \qquad \text{for} \quad T \leqslant t. \tag{2}$$

These results enable the volume of filtrate entering the horizontal layer, denoted by $\mathscr{V}(t)$, to be calculated. Equation (1) implies

$$\frac{\mathrm{d}\mathscr{V}(t)}{\mathrm{d}t} = \pi(r^2|_{z=H_{for}} - R_{wb}^2) W. \tag{3}$$

Substituting (2) into (3) and integrating, gives

$$\mathscr{V}(t) = \begin{cases} \pi R_{wb} u_f W t^2/\phi & \text{for} \quad t \leqslant T \\ 2\pi R_{wb} u_f H_{for}(t - T/2) & \text{for} \quad T \leqslant t. \end{cases} \tag{4}$$

These expressions are used in the analysis of the dynamics of the filtrate in the horizontal layer.

3. Horizontal layer analysis

3.1. *Modelling assumptions*

The analysis of the filtrate within the horizontal layer remains rather complex, even after decoupling it from the analysis of the vertical layer. For this reason, we have restricted our study to the dynamics of the filtrate located furthest from the wellbore, near the leading edge of the horizontal layer as it invades the formation, which will be referred to as the 'outer' region of the horizontal layer. This restriction is responsible for a major simplification in the analysis, modelling the source of filtrate entering the horizontal layer as coming from a point located at $(r, z) = (0, 0)$ having strength given by (3) or (4). It should be noted that restricting the analysis to the outer region is consistent with the fact that we are investigating the large-buoyancy case, as discussed in §1.

The point source has been located on the lower rather than on an upper horizontal impermeable solid boundary to facilitate comparison with our experimental results. Thus, the porous solid lies in the half-space $z > 0$, z-axis pointing in the direction opposite to gravity. However, there is no change in the physics other than inducing motion in the $-\hat{z}$, as opposed to the $+\hat{z}$, direction, equivalent to rotating figures 1 and 2 by 180° in the plane of the paper.

The dynamics of the filtrate is modelled by a rather simplified form of the multiphase Darcy law. Specifically, it is assumed that the filtrate completely displaces the formation fluid and capillary pressure effects can be ignored. The former assumption is quite good when the mobility (permeability of a particular phase divided by its viscosity) of the filtrate far exceeds that of the formation fluid, as is the case of a liquid displacing a gas. It is also a good approximation when the two phases are miscible, which is the case when water (oil) base drilling fluid invades a water (oil) zone, and is the situation in our experiments where the filtrate is a salt solution and the formation fluid consists of fresh water. The latter assumption, neglecting the capillary pressure, is justified when the lengthscale associated with the width of the transition region between the filtrate and the formation fluid, may be regarded as small relative to the other relevant lengthscales, or when the two phases are miscible.

Finally, we do not find a solution when the strength of the point source is given by (3) or (4), rather we focus on two special cases: $\mathscr{V}(t) \sim t^\alpha$, for $\alpha = 1, 2$. These should accurately describe the solution during early time ($\alpha = 2$), applicable when $0 \leqslant t < T$, and late time ($\alpha = 1$) asymptotically as $t \to \infty$, when $T < t$. The completeness of these two special cases in describing the desired point source is addressed in Part 2 where the dynamics of the filtrate in the vertical and horizontal layers are combined to describe invasion into the entire permeable zone.

3.2. *Scaling and expanding in a small parameter*

It is typical to begin an investigation by identifying the appropriate scales for all of the dependent and independent variables. However, in this problem many of the scales are not obvious, such as those associated with r, z, and the two components of velocity.

Instead, we know the material properties ρ_i, μ_i, k_h, k_v and ϕ, denoting respectively the densities and viscosities of both fluids (i represents either *for* or *fil*, denoting the formation fluid or filtrate, respectively), the horizontal and vertical components of the permeability of the porous solid (sedimentary rock, the porous solid of concern to us, is usually to some degree anisotropic, with $k_h/k_v > 1$) and the porosity of the solid. It is also assumed that a timescale, T, and the accumulative volume of filtrate which has entered the porous solid, at any time t, $\mathscr{V}(t)$, are known. In order to determine the appropriate scales, it is helpful to identify the boundary-value problem governing the dynamics of the fluids.

The governing equations and boundary conditions are as follows: Darcy's law (conservation of linear momentum) for both fluids,

$$0 = -\frac{\partial p_i}{\partial r} - \frac{\mu_i}{k_h} u_i, \tag{5}$$

$$0 = -\frac{\partial p_i}{\partial z} - \frac{\mu_i}{k_v} w_i - \rho_i g; \tag{6}$$

a combination of conservation of mass and the kinematic boundary condition at the filtrate–formation fluid interface (assuming the interface displaces all of the formation fluid as it moves through the formation),

$$\nabla \cdot \boldsymbol{u}_i = \phi c_i \frac{\partial p_i}{\partial t}, \tag{7}$$

$$\phi \frac{\partial \mathscr{Z}}{\partial t} + \frac{1}{r}\frac{\partial}{\partial r}\left(r \int_0^{\mathscr{Z}} u_{fil}\, \mathrm{d}z\right) = -c_{fil}\phi \int_0^{\mathscr{Z}} \frac{\partial p_{fil}}{\partial t}\, \mathrm{d}z, \tag{8}$$

$$\boldsymbol{u}_{fil} \cdot \boldsymbol{n} = \boldsymbol{u}_{for} \cdot \boldsymbol{n} \quad \text{at} \quad z = \mathscr{Z}(r, t); \tag{9}$$

the dynamic boundary condition at the filtrate–formation fluid interface,

$$p_{fil} = p_{for} \quad \text{at} \quad z = \mathscr{Z}(r, t); \tag{10}$$

the boundary condition at the impermeable surface of the solid,

$$w = 0 \quad \text{at} \quad z = 0; \tag{11}$$

boundary conditions far from the source,

$$p_{for} \to p_\infty - \rho_{for} g z \quad \text{as} \quad z^2 + r^2 \to \infty; \tag{12}$$

and a known volume of filtrate within the porous solid at time t,

$$\mathscr{V}(t) = 2\pi\phi \int_0^{R(t)} \mathscr{Z}(r, t)\, r\, \mathrm{d}r, \tag{13}$$

where $R(t)$ satisfies

$$0 = \mathscr{Z}(R(t), t), \tag{14}$$

attention being restricted to point sources resulting in filtrate volumes of the form $\mathscr{V}(t) = Qt^\alpha$, for $\alpha > 0$. Here c_i denotes the compressibility of each fluid; $\boldsymbol{u}$, equivalent to $u\hat{\boldsymbol{r}} + w\hat{\boldsymbol{z}}$, denotes the velocity of the fluids, $\hat{\boldsymbol{r}}$ and $\hat{\boldsymbol{z}}$ denoting unit vectors in the r- and

z-directions, respectively; $(r, \theta, \mathscr{Z}(r,t))$ denotes the location of the filtrate–formation fluid interface, with $\boldsymbol{n}$ denoting its local unit normal vector, and $R(t)$ denoting the radial position at which the fluid interface intersects the impermeable boundary, that is to say, the 'leading edge' of the filtrate as it spreads along $z = 0$.

This investigation has its limitations. Identifying the dominant terms in the above boundary-value problem consistent with these limitations determines the appropriate scales for the dependent and independent variables. Our principle restriction concerns the shape of the filtrate–formation fluid interface. It is assumed that the slope of the fluid interface is small relative to that of the impermeable solid boundary. Using a line of reasoning commonly employed in free-surface problems containing thin layers of liquids (the Navier–Stokes equation replacing Darcy's law), it is readily concluded that the small-slope assumption implies $\boldsymbol{u}_{for} \sim \boldsymbol{0}$, $\partial p_{ftl}/\partial r \sim \Delta\rho g H/L$ and $\boldsymbol{u}_{ftl} \sim U(H/L)\hat{\boldsymbol{r}}$, where U denotes $\Delta\rho g k_h/\mu_{ftl}$. Here, L and H represent, respectively, the yet to be determined scales for r and z in the filtrate, and $\Delta\rho$ denotes $(\rho_{ftl} - \rho_{for})$. The scaling is complete by making the following two assumptions: the two terms on the left-hand side of (8) be of comparable size, implying

$$\frac{\phi H}{T} = U\left(\frac{H}{L}\right)^2, \tag{15}$$

and each of the two terms in (13) be of comparable size, implying

$$QT^{\alpha} = \phi H L^2. \tag{16}$$

Equations (15) and (16) combine to give expressions for L and H in terms of known quantities,

$$L = (UQT^{\alpha+1}/\phi^2)^{\frac{1}{4}}, \tag{17}$$

$$H = (QT^{\alpha-1}/U)^{\frac{1}{2}}. \tag{18}$$

Thus, the scales chosen for the variables r, z, t, u, w and p are $L, H, T, UH/L, U(H/L)^2$ and $\Delta\rho g H$ for the filtrate, and $L, L(k_v/k_h)^{\frac{1}{2}}, T, U(H/L)^2, U(H/L)^2$ and $\Delta\rho g H$ for the formation fluid.

The boundary-value problem is expressed in dimensionless form based upon the above scales. A 'bar', or a 'hat', over a variable indicates respectively the use of the filtrate scale or the formation fluid scale. Equations (5)–(14) become: for the filtrate,

$$0 = -\frac{\partial \bar{p}}{\partial \bar{r}} - \bar{u}, \tag{19}$$

$$0 = -\frac{\partial \bar{p}}{\partial \bar{z}} - \epsilon^2 \bar{w} - \frac{\rho_{ftl}}{\Delta\rho}, \tag{20}$$

$$\frac{1}{\epsilon^2}\frac{\partial^2 \bar{p}}{\partial \bar{z}^2} + \frac{1}{\bar{r}}\frac{\partial}{\partial \bar{r}}\left(\bar{r}\frac{\partial \bar{p}}{\partial \bar{r}}\right) = \gamma_{ftl}\frac{\partial \bar{p}}{\partial \bar{t}}, \tag{21}$$

$$\frac{\partial \bar{\mathscr{Z}}}{\partial \bar{t}} + \frac{1}{\bar{r}}\frac{\partial}{\partial \bar{r}}\left(\bar{r}\int_0^{\bar{\mathscr{Z}}} \bar{u}\,\mathrm{d}\bar{z}\right) = -\gamma_{ftl}\int_0^{\bar{\mathscr{Z}}} \frac{\partial \bar{p}}{\partial \bar{t}}\mathrm{d}\bar{z}, \tag{22}$$

$$\bar{w} = 0 \quad \text{at} \quad \bar{z} = 0, \tag{23}$$

$$\bar{V}^{\alpha} = 2\pi \int_0^{R(\bar{t})} \bar{\mathscr{Z}}(\bar{r}, \bar{t})\,\bar{r}\,\mathrm{d}\bar{r}, \tag{24}$$

$$0 = \bar{\mathscr{Z}}(\bar{R}(\bar{t}), \bar{t}); \tag{25}$$

and for the formation fluid,

$$0 = -\frac{\partial \hat{p}}{\partial \hat{r}} - \frac{H}{L}\frac{\mu_{for}}{\mu_{fil}}\hat{u}, \tag{26}$$

$$0 = -\epsilon\frac{\partial \hat{p}}{\partial \hat{z}} - \epsilon^2\frac{\mu_{for}}{\mu_{fil}}\hat{w} - \frac{\rho_{for}}{\Delta\rho}, \tag{27}$$

$$\frac{\partial^2 \hat{p}}{\partial \hat{z}^2} + \frac{1}{\hat{r}}\frac{\partial}{\partial \hat{r}}\left(\hat{r}\frac{\partial \hat{p}}{\partial \hat{r}}\right) = \gamma_{for}\frac{\partial \hat{p}}{\partial \hat{t}}, \tag{28}$$

$$\frac{H}{L}\hat{u}\frac{\partial \bar{\mathscr{Z}}}{\partial \hat{r}} - \hat{w} = -\frac{\partial \bar{\mathscr{Z}}}{\partial \hat{t}} \quad \text{at} \quad \hat{z} = \epsilon\bar{\mathscr{Z}}(\bar{r}, \bar{t}), \tag{29}$$

$$\hat{p} = \bar{p} \quad \text{at} \quad \hat{z} = \epsilon\bar{\mathscr{Z}}(\bar{r}, \bar{t}), \tag{30}$$

$$\hat{p} \to \hat{p}_\infty - \frac{1}{\epsilon}\frac{\rho_{for}}{\Delta\rho}\hat{z} \quad \text{as} \quad \hat{z}^2 + \hat{r}^2 \to \infty. \tag{31}$$

Here, γ_i denotes the ratio of two timescales, $\mu_i \phi c_i L^2/k_h T$; ϵ denotes $(k_h/k_v)^{\frac{1}{2}}(H/L)$; and $\hat{p}_\infty$ denotes $p_\infty/\Delta\rho g H$. The other two dimensionless groups appearing in (19)–(31) are μ_{fil}/μ_{for} and $\rho_{fil}/\Delta\rho$. Note that k_h/k_v does not appear as an independent dimensionless group because of its inclusion in the scale for z in the formation fluid.

The small-slope assumption is formally imposed by seeking an asymptotic solution in the limit as $\epsilon \to 0$. The expansions of the dependent variables are as follows:

$$\bar{\mathscr{Z}} \sim \bar{\mathscr{Z}}_0(\bar{r}, \bar{t}; \gamma_i, \rho_{fil}/\Delta\rho, \mu_{fil}/\mu_{for}) + \epsilon\bar{\mathscr{Z}}_1 + \ldots, \tag{32}$$

$$\bar{R} \sim \bar{R}_0(\bar{t}; \gamma_i, \rho_{fil}/\Delta\rho, \mu_{fil}/\mu_{for}) + \epsilon\bar{R}_1 + \ldots, \tag{33}$$

$$\bar{p} \sim (1/\epsilon)\bar{p}_{-1}(\bar{r}, \bar{z}, \bar{t}; \gamma_i, \rho_{fil}/\Delta\rho, \mu_{fil}/\mu_{for}) + \bar{p}_0 + \epsilon\bar{p}_1 + \ldots, \tag{34}$$

$$\hat{p} \sim (1/\epsilon)\hat{p}_{-1}(\hat{r}, \hat{z}, \hat{t}; \gamma_i, \rho_{fil}/\Delta\rho, \mu_{fil}/\mu_{for}) + \hat{p}_0 + \epsilon\hat{p}_1 + \ldots, \tag{35}$$

requiring the latter two expansions to be consistent with both $\bar{u}$ and $\hat{u}$ being $O(1)$ as $\epsilon \to 0$. Here the higher-order terms in each of the above expansions depend upon the same variables as that indicated for the lowest-order term. In each expansion, all of the identified variables are held constant as $\epsilon \to 0$, except for γ_i, which are assumed to be $O(\epsilon)$.

3.3. *Solutions*

Determining the behaviour of the lower-order terms in the above asymptotic expansions is rather straightforward. Darcy's law for the filtrate, (19) and (20), and the assumption that $\bar{u}$ is of $O(1)$ as $\epsilon \to 0$, implies

$$\bar{p}_{-1} = \bar{A}_{-1}(\bar{t}), \tag{36}$$

$$\bar{p}_0 = -\frac{\rho_{fil}}{\Delta\rho}\bar{z} + \bar{A}_0(\bar{r}, \bar{t}), \tag{37}$$

while Darcy's law for the formation fluid, (26) and (27), and the assumption that $\hat{u}$ is of $O(1)$ as $\epsilon \to 0$, implies

$$\hat{p}_{-1} = -\frac{\rho_{for}}{\Delta\rho}\hat{z} + \hat{B}_{-1}(\hat{t}), \tag{38}$$

$$\hat{p}_0 = \hat{B}_0(\hat{t}). \tag{39}$$

The functions $\hat{B}_{-1}(\hat{t})$ and $\hat{B}_0(\hat{t})$ are determined from the boundary condition for the formation pressure far from the point source, (31), resulting in

$$\hat{p}_{-1} = -\frac{\rho_{for}}{\Delta\rho}\hat{z} \quad \text{and} \quad \hat{p}_0 = \frac{p_\infty}{\Delta\rho g H}, \tag{40}$$

and the functions $\bar{A}_{-1}(\bar{t})$ and $\bar{A}_0(\bar{r},\bar{t})$ are determined from the dynamic boundary condition at the fluid interface, (30), and (40), resulting in

$$\bar{p}_{-1}=0 \quad \text{and} \quad \bar{p}_0=-\frac{\rho_{fil}}{\Delta\rho}\bar{z}+\bar{\mathscr{Z}}_0+\frac{p_\infty}{\Delta\rho g H}. \tag{41}$$

Note that (40) and (41) are consistent with (28) and (21), respectively. The remaining lowest-order terms concern the shape of the fluid interface. The equation governing $\bar{\mathscr{Z}}_0$ follows directly by substituting (19) and (41) into (22), resulting in

$$\frac{\partial\bar{\mathscr{Z}}_0}{\partial\bar{t}}-\frac{1}{\bar{r}}\frac{\partial}{\partial\bar{r}}\left(\bar{r}\bar{\mathscr{Z}}_0\frac{\partial\bar{\mathscr{Z}}_0}{\partial\bar{r}}\right)=0, \tag{42}$$

subject to the constraint (24),

$$\bar{\ell}^\alpha=2\pi\int_0^{\bar{R}_0}\bar{\mathscr{Z}}_0(\bar{r},\bar{t})\,\bar{r}\,\mathrm{d}\bar{r}, \tag{43}$$

where $\bar{R}_0$ satisfies

$$0=\bar{\mathscr{Z}}_0(\bar{R}_0(\bar{t}),\bar{t}). \tag{44}$$

The boundary-value problem defined by (42), (43) and (44) has been investigated by Barenblatt (see Barenblatt *et al.* 1990). He obtained a similarity solution for $\bar{\mathscr{Z}}_0$ of the form

$$f\equiv\frac{(2\pi)^{\frac{1}{2}}\bar{\mathscr{Z}}_0}{\eta_R^2\,\bar{t}^{\frac{\alpha-1}{2}}} \tag{45}$$

and

$$\eta\equiv\frac{(2\pi)^{\frac{1}{4}}\,\bar{r}}{\eta_R\,\bar{t}^{\frac{\alpha+1}{4}}}, \tag{46}$$

where f satisfies the ordinary differential equation

$$-\frac{\alpha+1}{4}\eta\frac{\mathrm{d}f}{\mathrm{d}\eta}+\frac{\alpha-1}{2}f-\frac{1}{\eta}\frac{\mathrm{d}}{\mathrm{d}\eta}\left(\eta f\frac{\mathrm{d}f}{\mathrm{d}\eta}\right)=0 \quad \text{for} \quad 0<\eta\leqslant 1, \tag{47}$$

subject to the boundary condition

$$f(1)=0, \tag{48}$$

and η_R is given by

$$\frac{1}{\eta_R^4}\equiv\int_0^1 f\eta\,\mathrm{d}\eta. \tag{49}$$

As Barenblatt noted, it is convenient to have an additional boundary condition for f at $\eta=1$, when obtaining a numerical solution of (47). This is accomplished by generating an asymptotic solution to (47) about $\eta=1$, in terms of a power series in $1-\eta$, resulting in

$$f\sim\frac{\alpha+1}{4}(1-\eta)+\frac{\alpha-1}{8}(1-\eta)^2+\frac{(\alpha+3)\alpha}{36(\alpha+1)}(1-\eta)^3+\ldots, \tag{50}$$

implying

$$\frac{\mathrm{d}f}{\mathrm{d}\eta}=-\frac{\alpha+1}{4} \quad \text{at} \quad \eta=1. \tag{51}$$

Numerical solutions have been obtained to the initial-value problem defined by (47), (48) and (51) using the ordinary differential equation solver, based upon fourth- and fifth-order Runge–Kutta formulae, available on *MATLAB*^{TM}; refer to figure 3. Values

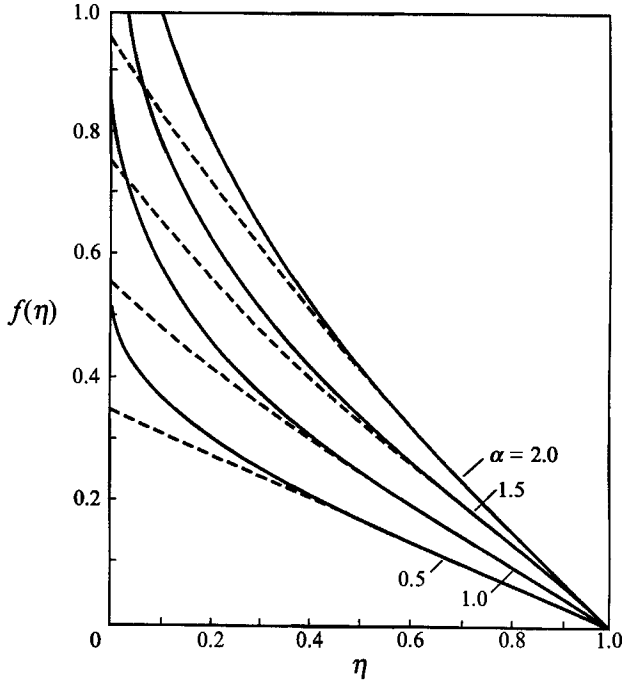

FIGURE 3. The solution for $f(\eta)$. The solid curves indicate the exact numerical solution over a range of value of α. The dashed curves represent the asymptotic solution given by (50).

α	η_R	η_R^*	α	η_R	η_R^*
0.1	2.2744	2.2824	1.9	1.6338	1.6508
0.2	2.1919	2.2036	2.0	1.6177	1.6347
0.3	2.1234	2.1371	2.5	1.5478	1.5645
0.4	2.0650	2.0799	3.0	1.4908	1.5073
0.5	2.0141	2.0298	3.5	1.4430	1.4592
0.6	1.9691	1.9853	4.0	1.4020	1.4180
0.7	1.9288	1.9454	4.5	1.3662	1.3820
0.8	1.8925	1.9092	5.0	1.3346	1.3502
0.9	1.8594	1.8763	5.5	1.3063	1.3217
1.0	1.8290	1.8460	6.0	1.2809	1.2960
1.1	1.8010	1.8181	6.5	1.2577	1.2726
1.2	1.7751	1.7922	7.0	1.2364	1.2512
1.3	1.7510	1.7681	7.5	1.2169	1.2315
1.4	1.7284	1.7455	8.0	1.1988	1.2133
1.5	1.7072	1.7243	8.5	1.1820	1.1963
1.6	1.6873	1.7043	9.0	1.1663	1.1805
1.7	1.6685	1.6855	9.5	1.1516	1.1656
1.8	1.6507	1.6677	10.0	1.1377	1.1516

TABLE 1. Evaluation of η_R and η_R^*

for η_R have been evaluated from these solutions using (49); refer to table 1. Also included in table 1 are values of η_R obtained using the asymptotic solution (50), which are denoted by η_R^*.

These values of η_R differ by about 10% from those calculated using Barenblatt's solution. Presumably, this reflects the better computational resources available today

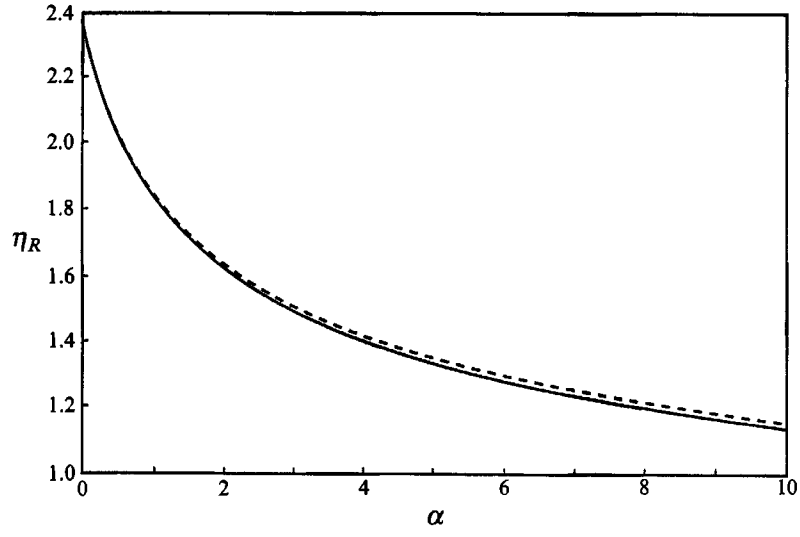

FIGURE 4. The solutions for η_R (——) and η_R^* (– – –) over a range of values of α.

as compared to 40 years ago, when he first published his results. It is of interest to note the extent to which the sum of the first three terms of the asymptotic expansion of f follows the exact solution, refer to figure 3, as well as the degree to which η_R^* agrees with η_R, refer to table 1 and figure 4.

4. Experiment

Images were taken, using the X-ray CT scanner, of the filtrate as it progressed through the porous solid. Detection and digitization of the location of the filtrate–formation fluid interface were accomplished using a simple pattern recognition technique. This section begins with a description of the instrumentation, and a characterization of the materials used in the experiment (the porous solid, the filtrate and the formation fluid), followed by a detail description of the pattern recognition technique used to interpret the X-ray attenuation images produced by the X-ray CT scanner. Then the experimental procedure is presented, along with the calibrations of the measurements and the results.

4.1. *Instrumentation*

The X-ray CT scanner was made by Elscint, model Exel 2002 BiModal CT, designed for medical purposes. It contains an X-ray tube which operates at a continuous high voltage of 140 kV and a current of 42 mA. Its innovative bimodal design utilizes a sequence of five coplanar translations of the radiation-detection system, each performed at a different angle relative to the sample. The radiation-detection system consists of an X-ray source producing a fan-shaped beam, opposed by a row of detectors, both lying in the same plane as the five coplanar translations of the system. The sample was placed so that the specific cross-section being imaged coincided with the plane of the radiation-detection system, the sample lying between the X-ray source and detectors. The thickness of the detected cross-section was 5 mm, determined by the thickness of the fan-shaped beam emitted by the X-ray source. The resolution of the images (in the plane of the image) was approximately 1 mm, determined by the size and number of detectors. An entire scan took one minute. Each image consisted of a

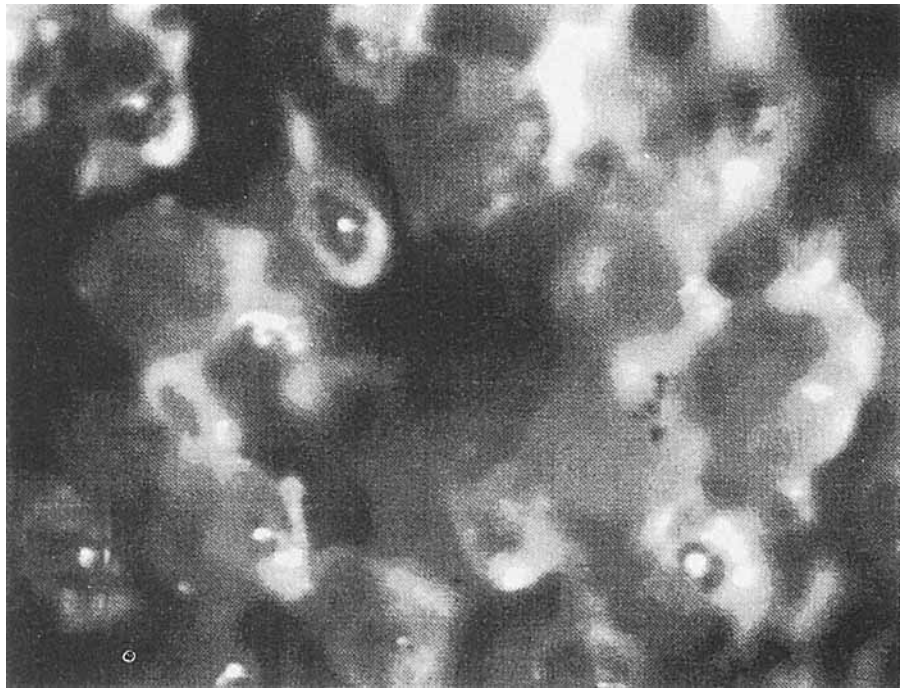

FIGURE 5. Image of a fractured surface of the porous solid on the microscopic scale. The resin (light regions) coats and consolidated the glass beads (shiny spherical regions). The darker regions are part of the pore.

512 × 512 numeric matrix of the X-ray attenuation data which was processed remotely on a Sun Sparc 2 station using KBVision^{TM} (image analysis software developed by Amerinex Artificial Intelligence of Amherst MA).

A Harvard syringe pump delivered filtrate at a constant volumetric flow rate to the sample. The syringe had a capacity of 250 ml, and the volumetric flow rate was known to within 2%. An analytic balance manufactured by A&D Engineering was used to monitor the amount of liquid exiting the sample through the Plexiglas chamber during the course of each experiment. The viscosity of the fluids was measured using a Cannon-Fenske viscometer.

4.2. *Characterization of the porous solid*

The porous solid was a composite structure having a relative high porosity and permeability composed of resin-cemented 100 um diameter glass beads, sold commercially as a filter (Eaton Products, Birmingham Michigan). Figure 5 is an image of the material. Each experiment was conducted using the same porous solid sample, a 'pie-shaped' sector cut from a cylinder, shown in figure 6. Each flat face of the sample was sealed with epoxy. The one remaining curved face was left unsealed so that the liquid could freely leave the sample. A Plexiglas chamber was attached to this end, which extended over the entire curved surface, to collect the exiting liquid and to maintain a hydrostatic pressure distribution (figure 7). The filtrate was delivered to the sample by $\frac{3}{16}$ in. (ID) nylon tubing. A branch, which served as a purge, was created in the tubing a few centimetres upstream from the sample. Values were inserted, one in the branch, another upstream from the sample and downstream from the branch. The 'point source', the position of entry of the filtrate into the porous solid, consisted of

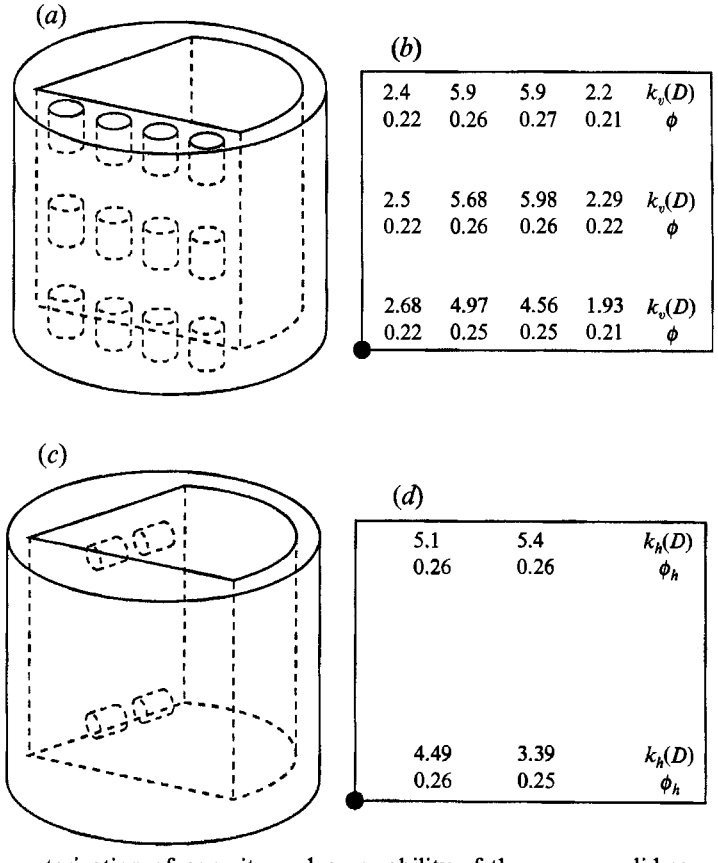

FIGURE 6. Characterization of porosity and permeability of the porous solid sample A pie-shaped sector was cut from a cylindrical block of porous material as indicated in (*a*) and (*c*). Also shown are the cores removed from the remaining material originally adjacent to both flat surfaces of the pie-shaped sector, whose porosity, ϕ, and vertical or horizontal permeability, k_v or k_h, were measured. The values are shown in (*b*) and (*d*). Note the position of the point source at the lower left corner of (*b*) and (*d*).

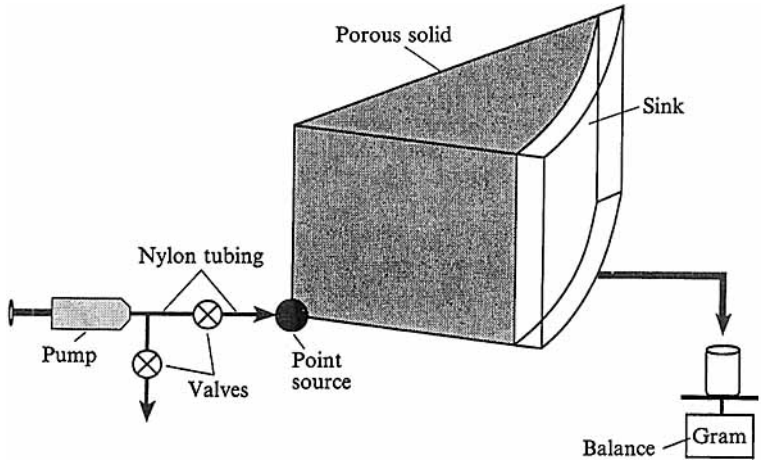

FIGURE 7. Schematic of the experimental set-up.

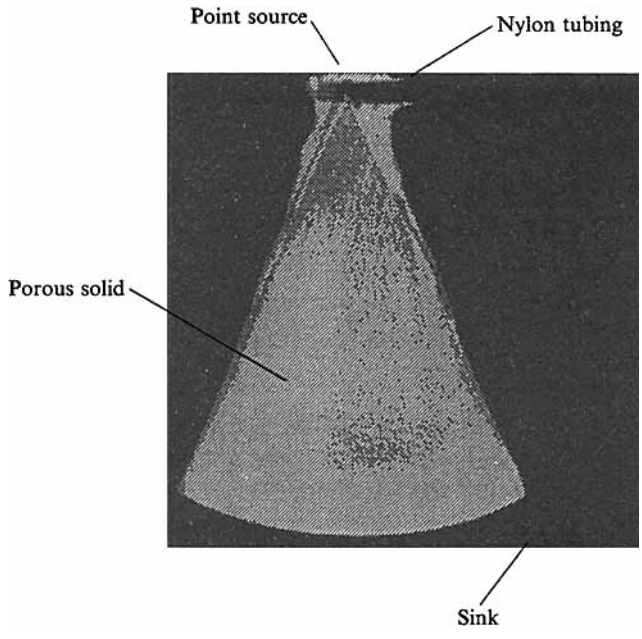

FIGURE 8. X-ray attenuation image of sample indicating the location and structure of the point source. The image is taken of a plane located at an elevation, z = constant, just above the lower impermeability boundary.

an opening in the nylon tubing positioned on the sample at the lowest point along the edge created by the intersection of the two vertical sides of the wedge. It is visible in the X-ray attenuation image of the sample of figure 8. The location of the point source is also indicated by the small bright region at the lower left corner of the image in figure 9, representing a 'side view' inside the sample. The outer radius of the pie-shaped sample, i.e. the distance between the point source and the curved face (figure 9), was 12.3 cm and the height of the sample was 12 cm.

The physical properties of the porous solid were determined from measurements performed on horizontal and vertical Hassler cores taken from that part of the remains of the cylindrical filter which were contiguous to the two flat sides of the wedge of the sample, as indicated in figure 6. The permeability and porosity of each core were measured, their values are also indicated in the figure. Notice the degree of heterogeneity in the sample, a characteristic also of sedimentary rock. Since the theory assumes a homogeneous porous solid, the porosity and horizontal permeability were averaged over the lower portion of the sample, the location of the filtrate during the experiments, giving values of 0.255 and 4765 mD, respectively.

4.3. *Characterization of filtrate and formation fluid*

The criterion for choosing the filtrate and the formation fluid (beyond the fact that they have different densities and are miscible) was to maximize the difference in X-ray attenuation attained within regions of the porous solid fully saturated with each fluid. Various expressions for the X-ray attenuation, μ_{CT}, have appeared in the literature (Evans 1955; Ellis 1987; Wellington & Vinegar 1987). They all indicate a dependence of μ_{CT} upon the energy E of the X-ray, the average density ρ and mass-fraction-weighted average atomic number $\bar{Z}_{CT}$, of the following form:

$$\mu_{CT} = \alpha_{CT}(E) + \beta_{CT}(E)\,\rho + \gamma_{CT}(E)\,\rho\,\bar{Z}_{CT}^{m}, \tag{52}$$

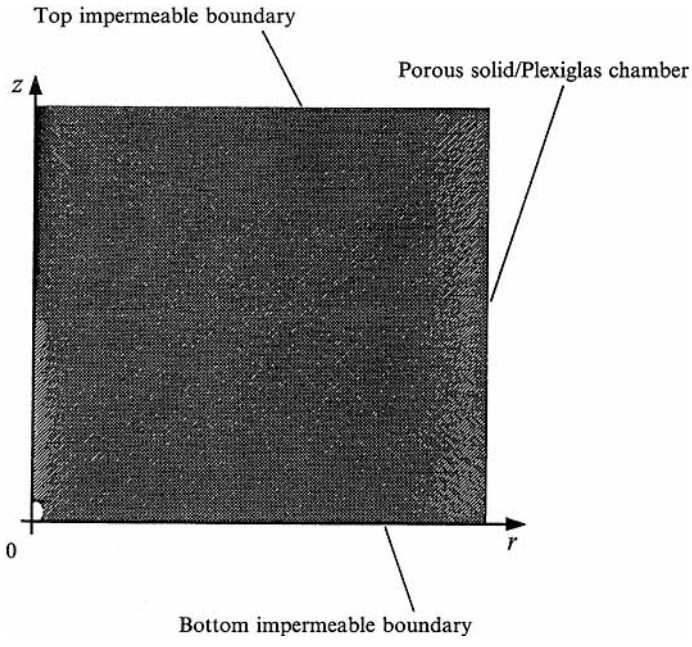

FIGURE 9. X-ray attenuation image of a plane located at ϕ = constant, corresponding to about half the angle of the sector of the sample. The upper and lower impermeable boundaries correspond to the top and bottom edges of the image. The porous solid/Plexiglas chamber boundary corresponds to the right edge of the image. The location of the source of filtrate is $(r, z) = (0, 0)$.

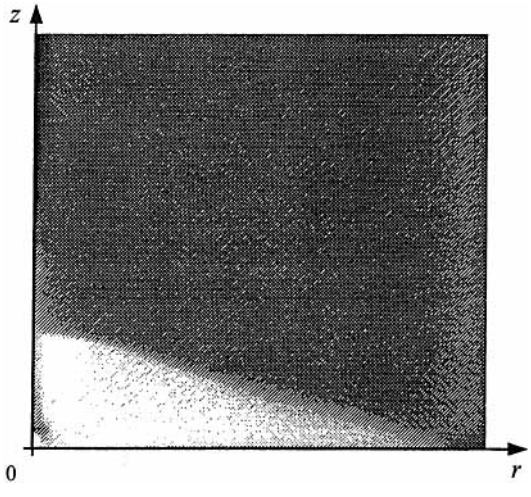

FIGURE 10. X-ray attenuation image of the invaded sample. The filtrate (light grey) is denser than the formation water (dark grey).

where $\alpha_{CT}(E)$, $\beta_{CT}(E)$ and $\gamma_{CT}(E)$ are energy-dependent coefficients, and m ranging in value from 3 to 4 for porous rock. Advantage was taken of the sensitivity of μ_{CT} to $\bar{Z}_{CT}$ by choosing a solution of sodium bromide and distilled water for the filtrate, having density of 1.4 g/cm^3, and distilled water alone for the formation fluid. Sodium bromide was selected because its atomic number is 4.6 time greater than that of water. The viscosity of the filtrate was measured to be 1.93×10^{-2} P.

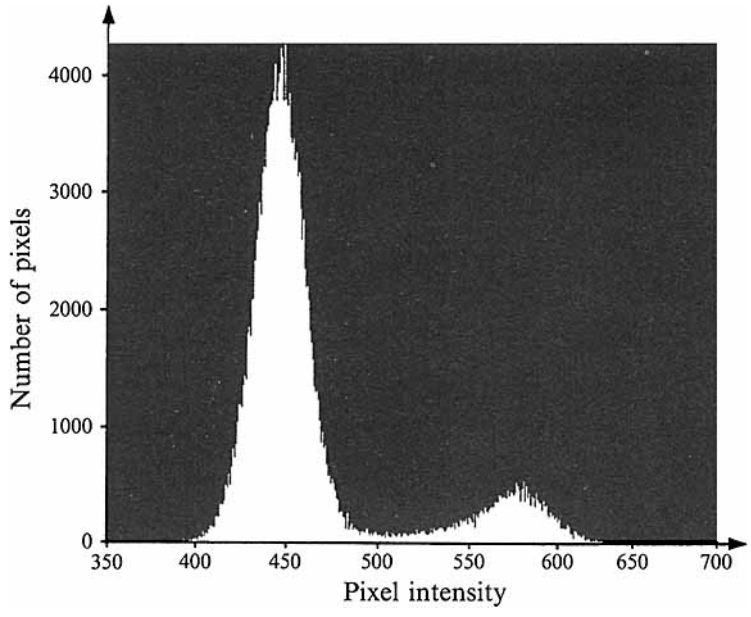

FIGURE 11. Histogram of the pixel intensities in a typical X-ray attenuation image of the sample containing both invaded filtrate and formation fluid. The small peak at the high pixel intensity corresponds to the filtrate, and the large peak at the intermediate pixel intensity corresponds to the formation fluid.

4.4. *Pattern recognition*

To identify the location of the invading filtrate front, a technique based on pattern recognition was developed. The problem was to find the boundary between the filtrate and the formation fluid. These are two adjacent regions, each showing good contrast (figure 10), as indicated by the one-dimensional histogram of the intensity of the pixels in the image (figure 11). The histogram shows two distinct peaks, the first centred at a pixel intensity of 450 corresponding to the X-ray attenuation of the saturated sample without invading fluid (called the background region), and the second smaller peak, centred at a pixel intensity of 575, due to the presence of the invading fluid in the sample. The clear separation between the X-ray attenuations caused by the formation fluid and the invading fluid makes it possible to remove the signal associated with the background region. A plot of the pixel intensity at each position within the image (figure 12) shows a large peak at the origin due to the invading fluid in the point source. Adjacent to this peak is a region of constant, but smaller, pixel intensity (a plateau) corresponding to the sample invaded solely by the filtrate fluid. This plateau of constant intensity is bordered by a region characterized by a gradual decrease in intensity (appearing as a sloped surface) suggesting a transition between the filtrate and the formation fluid within the sample. This gradual transition is then followed by another plateau representing the region where no invading fluid is present. This indicates that there is no sharp interface between the formation fluid and the filtrate. This motivated us to determine the approximate locations of the boundary of the diffuse layer at the filtrate front, i.e. the upper and lower edges of the sloping surface.

Given the above characteristics of the image, a simple thresholding approach was implemented. This consisted of identifying two values of the pixel intensity corresponding to the filtrate and the formation, as represented by the height of each plateau in figure 12. To remove the systematic errors associated with the sample

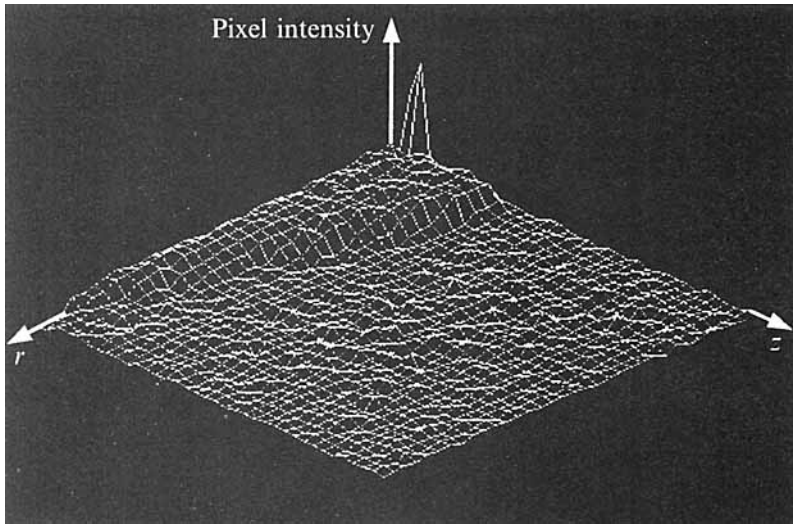

FIGURE 12. Plot of the pixel intensities comprising a typical image. The r-axis coincides with the lower impermeable boundary. The z-axis coincides with the 'sharp edge' of the pie-shaped sample.

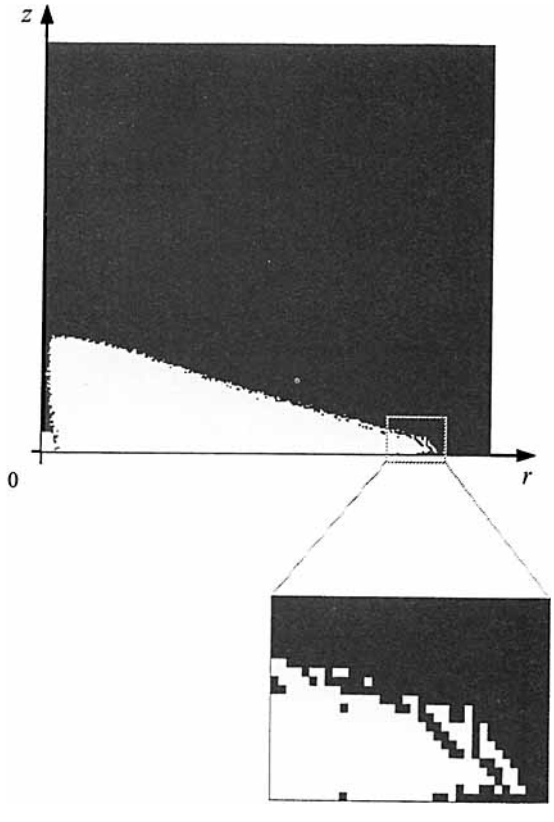

FIGURE 13. Binary image of the invaded sample. Note the many disconnected regions, refer to enlarged portion of the image.

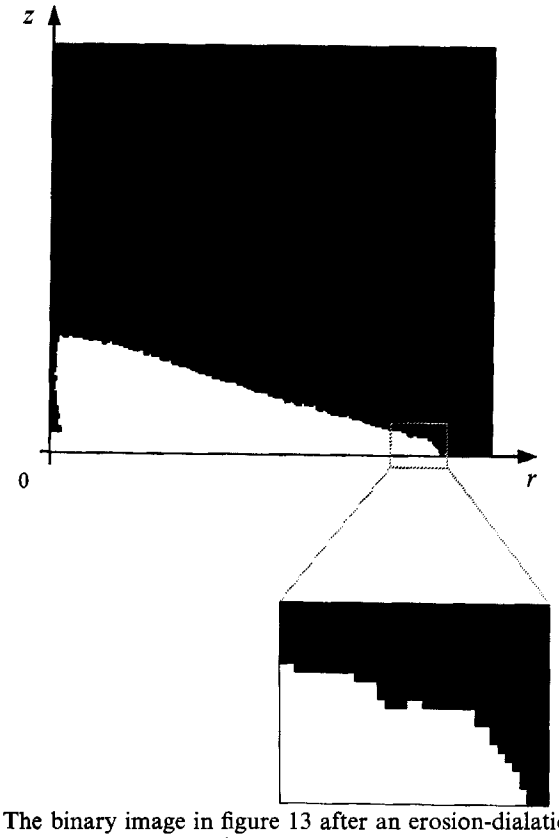

FIGURE 14. The binary image in figure 13 after an erosion-dialation algorithm has been performed.

saturated with formation fluid, the first image (figure 9), taken before the injection of the filtrate, was subtracted from every later image. A detailed description of choosing the thresholds is given below. These thresholds were used to compute two binary images. Each resultant binary image (figure 13) showed the region of interest (either the lower or the upper parts of the boundary of the diffuse layer at the filtrate front) with many subregions (or 'holes') in it resulting from the distribution of pixel intensity within the two plateaus referred to above. To simplify the pattern recognition process, the images were dilated to remove these detached subregions. This resulted in moving the edge of the invading fluid outward into the formation fluid by a few pixels. An erosion algorithm was then necessary to move the edge back to its original position (figure 14). The last step was to convert the two binary images into data (often referred to as a 'token') representing the approximate locations of the two boundaries of the diffuse layer. We converted each binary image to its token representation using commercial software (figure 15). This technique reduced the storage requirement by replacing each image of approximately half a megabyte by a token consisting of two kilobytes.

In order to implement the pattern recognition technique, the values of the thresholds had to be identified. This was done in the following way. The pattern recognition algorithm was executed using an image taken near the conclusion of one of our reported experiments. This was done over a range of threshold settings spanning the intensity of the pixels within the diffuse region. At every intensity level within this range, the shape and location of each recognized curve and the volume within the

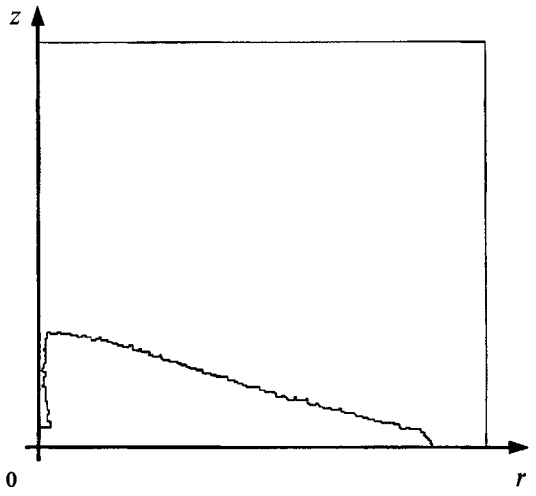

FIGURE 15. The token representation of the binary image in figure 14.

sample, beneath each recognized curve, were determined (figure 16). Despite the erosion and dialation of the image in the pattern recognition technique, relatively large or small thresholds within the range produced rather complicated shapes, as indicated by threshold values of 45 and 230 in figure 16(*b*). The thresholds which were chosen to be used when analysing the images were the largest and smallest pixel intensities which recognized relatively smooth curves, 65 and 195 in figure 16(*c*). (Actually, the value of the larger threshold was reduced to eliminate the apparent artifact along the bottom of the images.) The levels of the pixel intensity of the images taken during other experiments were adjusted so that the intensities of the two peaks in the histograms were all at the same value. Having 'normalized' the scale of the intensity for all our images, the same thresholds were used throughout the entire study.

4.5. *Experimental procedure*

Preparation for the experiments began by saturating the sample with distilled water. This was done under vacuum in a tank, resulting, at the conclusion of this procedure, in the sample being fully immersed in water. Without moving the sample, the tubing from the syringe pump was attached to it at the point source. When making this connection, the syringe pump was on, injecting water through the tubing and out of its ends (one end connected to the sample the other end of the purge) to insure that no air bubbles would get trapped. A piece of tubing was also connected, at this time, to the Plexiglas chamber situated along the curved surface of the sample, through which the distilled water leaves the sample. With the syringe pump maintained on, the purge was closed and the tubing leaving the chamber was placed below the water–air interface in a beaker (situated on the analytic balance). Only then was the sample removed from the tank and positioned in the X-ray CT scanner and the pump shut off. The syringe was filled with the sodium bromide solution by first closing the valve just upstream of the sample, opening the valve at the purge, emptying the distilled water from the syringe through the purge, refilling the syringe with solution and, finally, closing the valve at the purge.

The experiments began by activating the syringe pump in its injection mode while having the valve to the sample closed and the purge open. The X-ray CT scanner was then used to check the position of the porous medium and to obtain an image of the

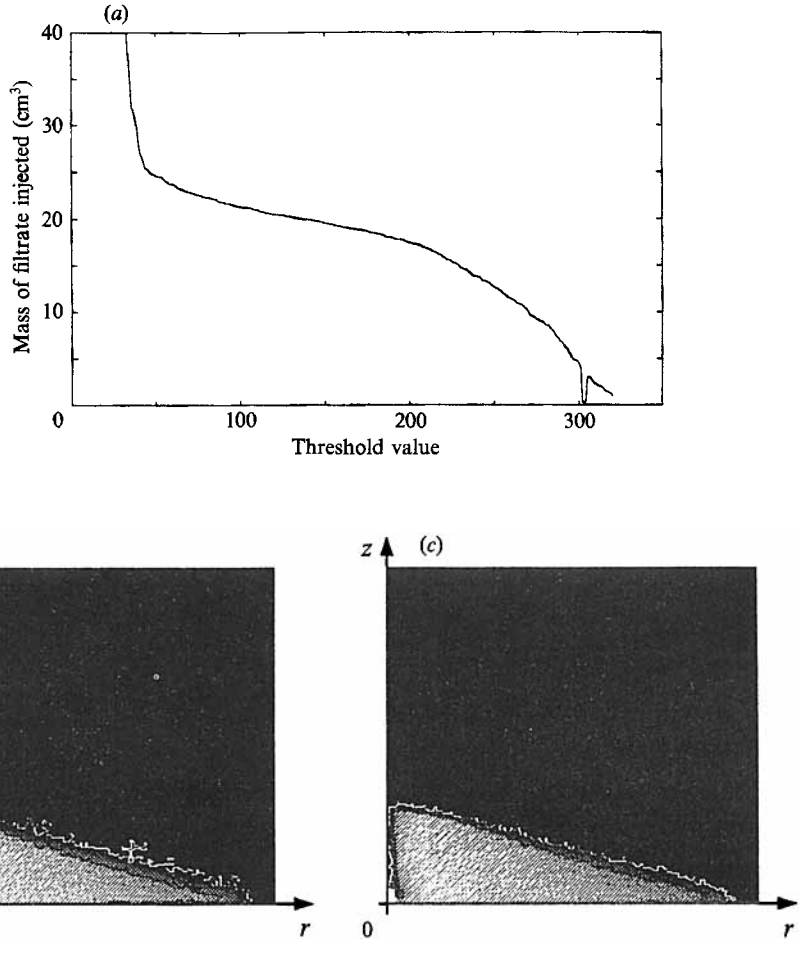

FIGURE 16. Recognizing the diffuse region situated between the filtrate and the formation fluid. The volume beneath the recognized curve over a range of threshold values for a typical X-ray image are given in (*a*). The location within the image of the recognized curves are given for threshold values of 45 and 230 in (*b*) and 65 and 195 in (*c*).

sample saturated with only distilled water. With the pump continuously running in the above-stated configuration, the purge was closed while the valve just upstream of the sample was simultaneously opened. All of this was accomplished using remote controls so that an image could be taken simultaneously with the scanner. This corresponded to the time at which the experimental clock began. Subsequent images were taken every minute at the beginning of the experiment, with larger time intervals between images as the experiment progressed. An average of sixty images were taken for each experiment. Throughout each experiment, the temperature in the scanner room was maintained at 21 °C. At the conclusion of each experiment, the syringe was filled with distilled water and the sample flushed until approximately one gallon of water passed through. This was done with the sample rotated 90° from its orientation in the X-ray CT scanner so that its curved surface faced the floor. All of the experiments were carried out using the same sample.

The above-described experimental procedure has the undesirable characteristic that $t = 0$ did not coincide with the initial appearance of filtrate in the sample at the

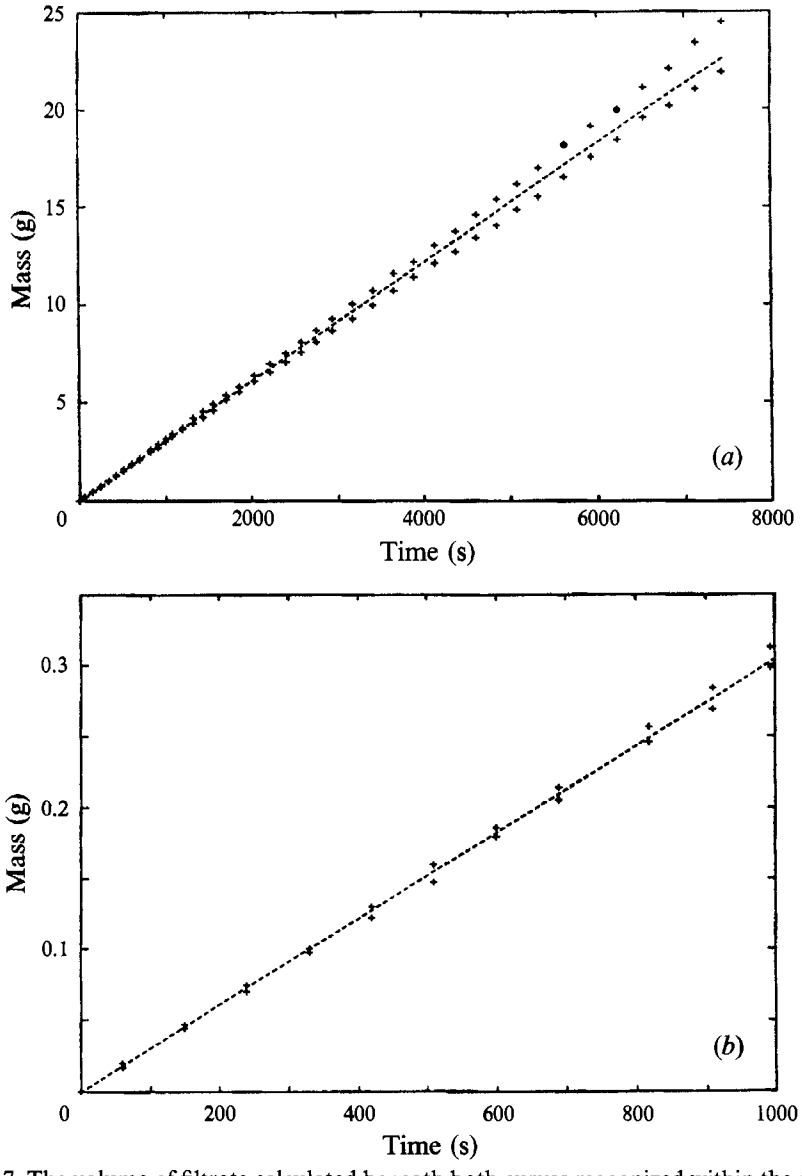

FIGURE 17. The volume of filtrate calculated beneath both curves recognized within the diffuse region compared to the measured mass of fluid displaced from the sample; see figure 18. The injection rate in this experiment was 3.0×10^{-3} cm^3/s and the time was shifted by 60 s.

beginning of each experiment. This was a direct consequence of the location of less than one half a cubic centimeter of distilled water just ahead of the sodium bromide in the portion of the tubing between the sample and the nearest valve. To compensate for this injected volume, the moment corresponding to $t = 0$ was shifted in each experiment to the time that the filtrate began entering the sample, i.e. the shift was equivalent to making the volume of filtrate determined from the images to extraporlate to zero at time $t = 0$. The extrapolation was done using the fact that fluid always entered the sample at a constant volumetric flow rate (substantiated by the continuous monitoring of the weight of the fluid leaving the sample). Figure 17, typical of all our experiments, compares the volume of filtrate calculated beneath both curves recognized

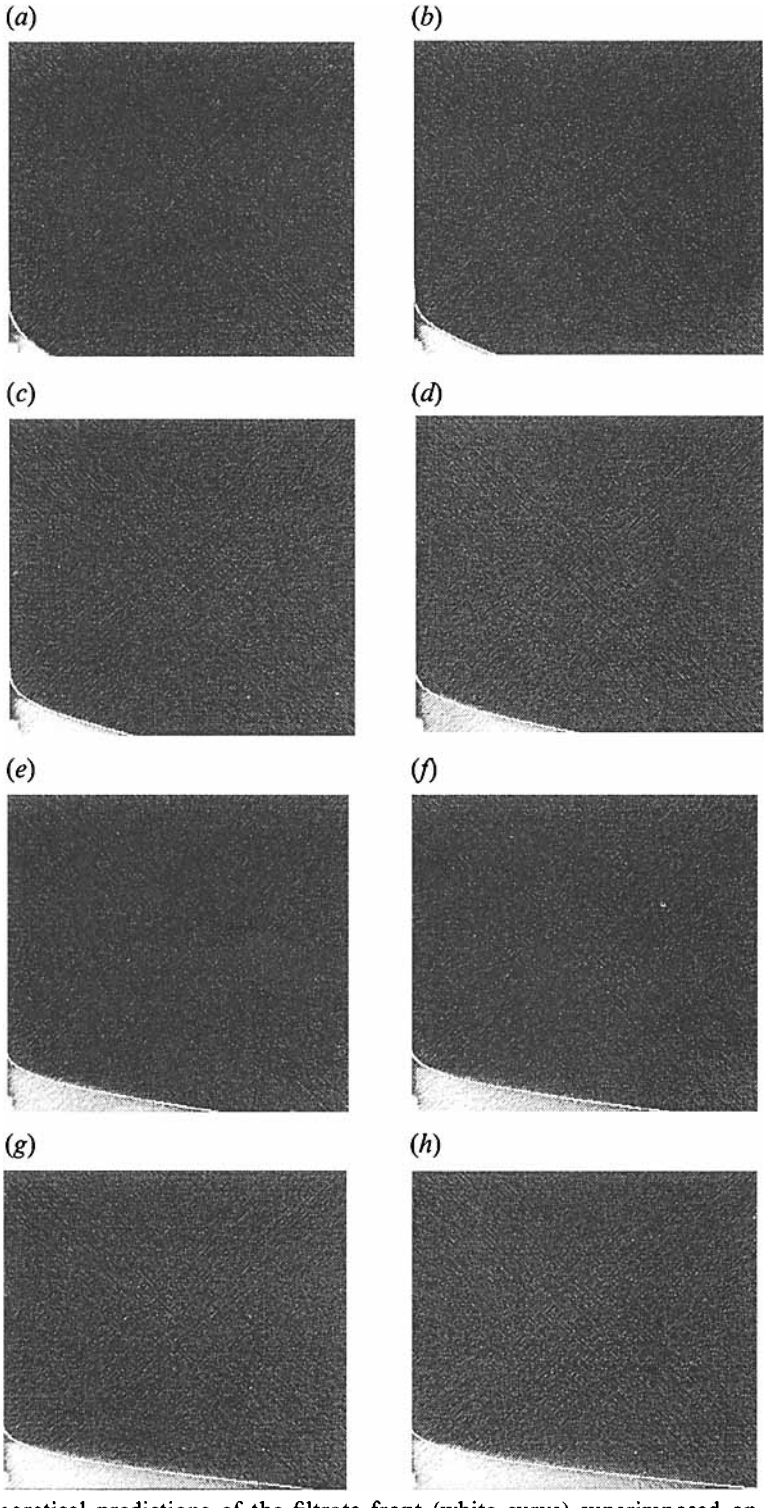

FIGURE 18. Theoretical predictions of the filtrate front (white curve) superimposed on the X-ray attenuation images taken at eight different times: (*a*) $t = 250$ s, (*b*) $t = 1090$ s, (*c*) $t = 2290$ s, (*d*) $t = 3970$ s, (*e*) $t = 7000$ s, (*f*) $t = 10030$ s, (*g*) $t = 14350$ s, (*h*) $t = 17950$ s. The injection rate was 5.2×10^{-4} cm^3/s.

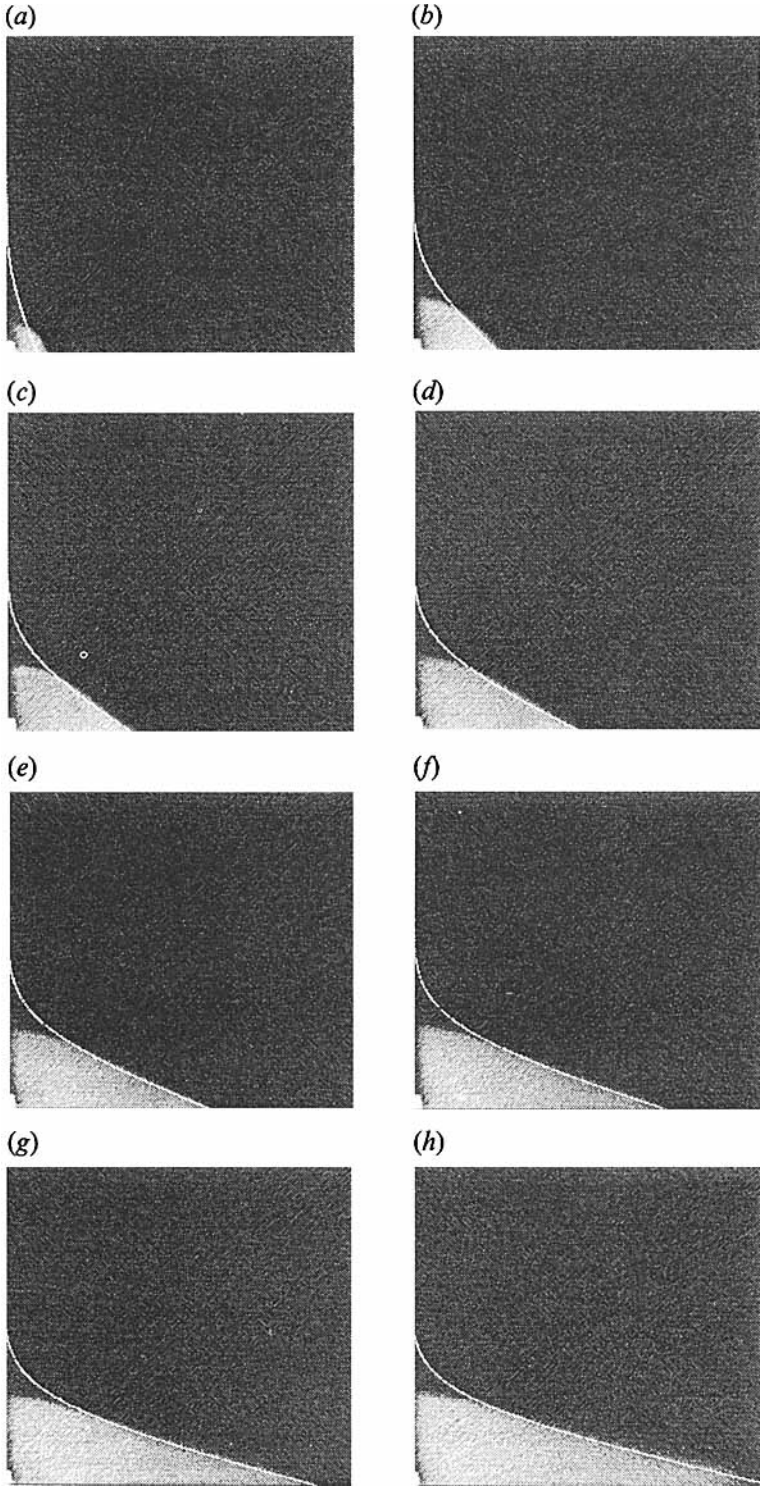

FIGURE 19. As figure 18 but at times: (*a*) $t = 60$ s, (*b*) $t = 420$ s, (*c*) $t = 910$ s, (*d*) $t = 1560$ s, (*e*) $t = 2400$ s, (*f*) $t = 3660$ s, (*g*) $t = 5640$ s, (*h*) $t = 7740$ s and for injection rate 3.0×10^{-3} cm^3/s.

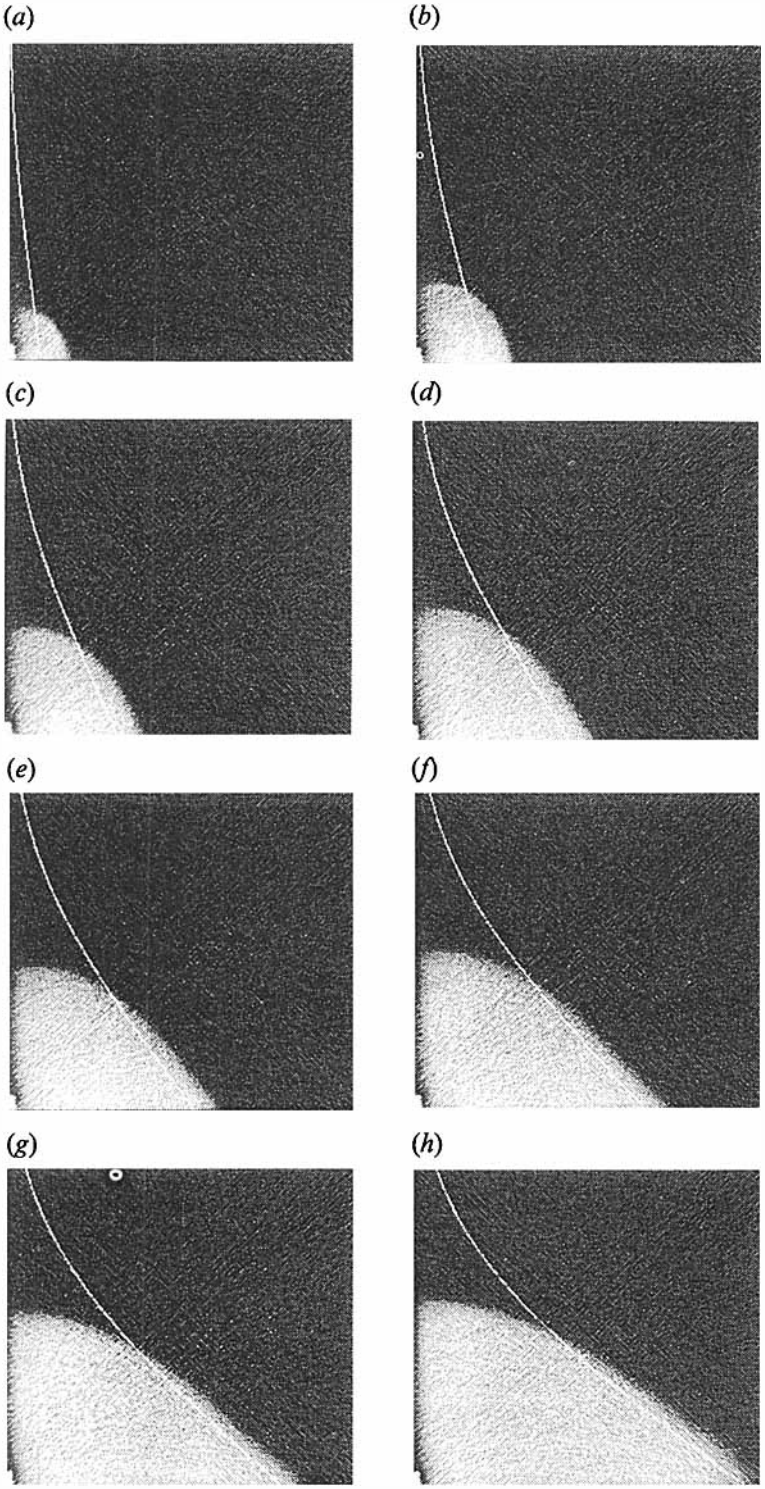

FIGURE 20. As figure 18 but at times: (*a*) $t = 26$ s, (*b*) $t = 111$ s, (*c*) $t = 276$ s, (*d*) $t = 519$ s, (*e*) $t = 728$ s, (*f*) $t = 1137$ s, (*g*) $t = 1571$ s, (*h*) $t = 2231$ s and for injection rate 2.5×10^{-2} cm^3/s.

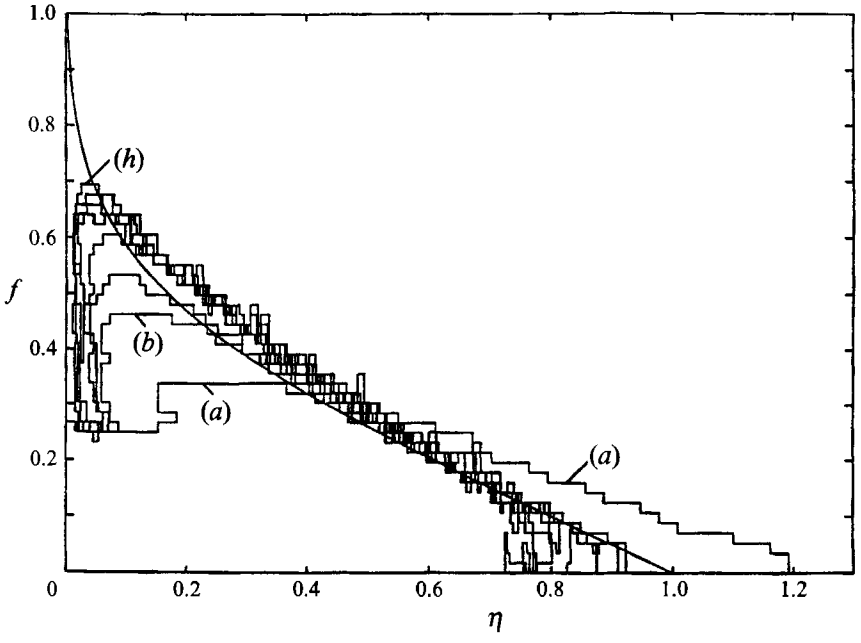

FIGURE 21. Theoretical prediction along with the eight recognized filtrate fronts (corresponding to the smaller of the two thresholds) obtained from the images in figure 18.

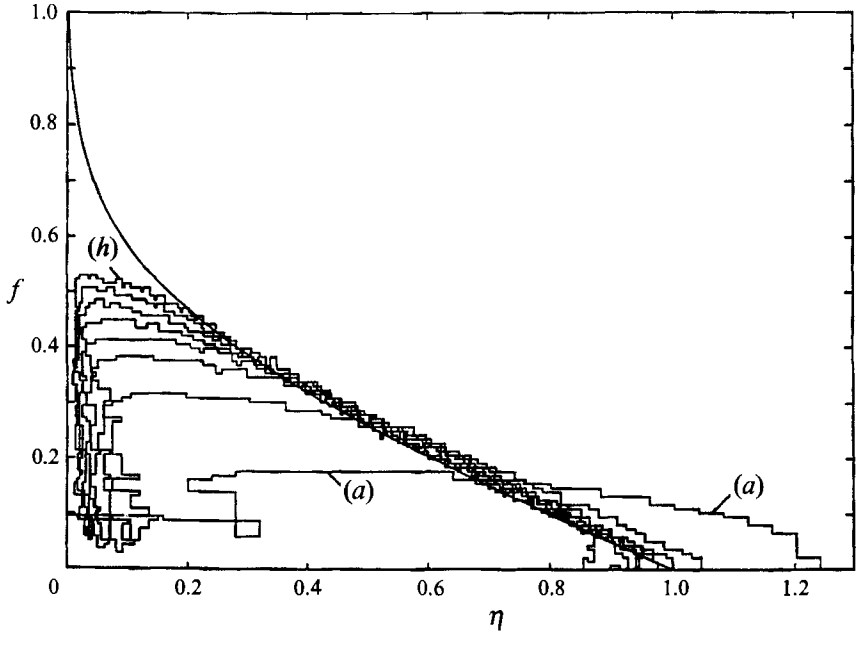

FIGURE 22. As figure 21 but obtained from the images in figure 19.

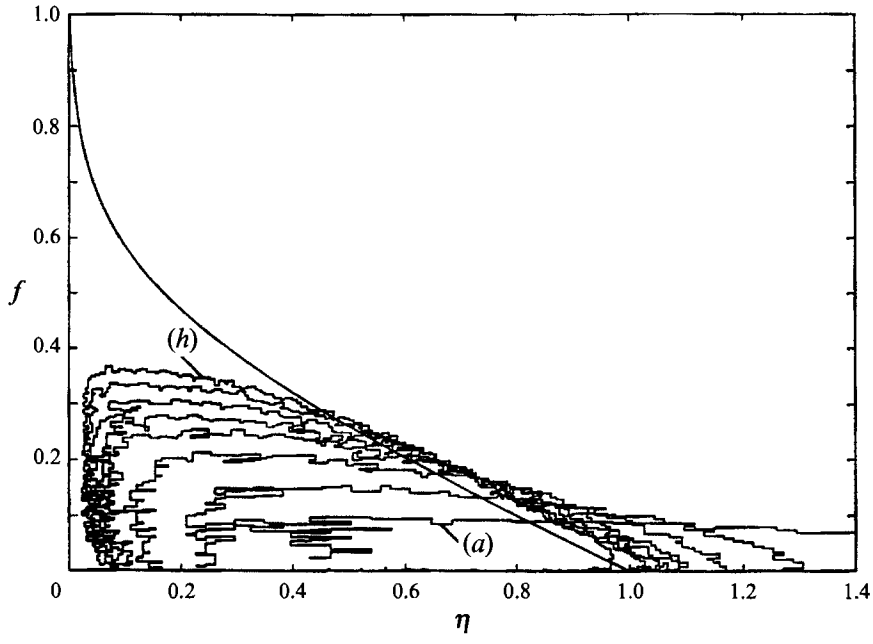

FIGURE 23. As figure 21 but obtained from the images in figure 20.

within the diffuse region of every image taken during an experiment and the measured mass of the fluid displaced from the sample by the injected filtrate after shifting the moment corresponding to $t = 0$.

4.6. *Results*

The results of three experiments are presented, each corresponding to a different filtrate volumetric flow rate: 5.2×10^{-4}, 3.0×10^{-3} and 2.5×10^{-2} cm^3/s. Four X-ray CT scanner images taken at different times, for each experiment, are displayed in figures 18, 19 and 20 in a grey scale representation of the X-ray attenuation data. The brighter the pixel, the larger the attenuation coefficient, and hence, the denser the fluid. Thus lighter regions indicate filtrate, while darker regions indicate the presence of distilled water. The position at which the filtrate was injected into the sample appears as a bright circle at the lower left corner of each image, and the solid white curve represents an evaluation of the theoretical results assuming $\alpha = 1$. Finally, the suite of recognized curves (corresponding to the smaller of the two thresholds) for the four images associated with each experiment, re-expressed in terms of (η, f) using (45) and (46), appear in figures 21, 22, and 23.

5. Discussion and conclusions

The focus of this study has been on the dynamics of the filtrate only in the horizontal layer, which is part of the larger problem of filtrate invading a permeable bed from a wellbore. By further restricting our attention to the outer region of the horizontal layer, we identified and investigated, both experimentally and theoretically, the specific problem consisting of a point source of filtrate located on an otherwise impermeable horizontal boundary of a fully saturated porous medium. We shall now use the experimental results to evaluate the appropriateness and limitations of some of the simplifying assumptions employed in the theoretical analysis of this specific problem.

Probably the most unexpected result has been the robustness of the solution, in spite of the small-slope approximation. This is evident in figures 20 and 23 which indicate adequate agreement even when rather large slopes are present. However, the extent of the agreement in the radial direction is not the same in all cases. The experiments indicate that the smaller the slope at the filtrate's leading edge, then the greater the region of agreement in r, refer to figures 18–23.

It should be no surprise that the theory breaks down near the origin, above the point source, as indicated in figures 18–23. Here, it can be concluded, based upon physical reasoning, that the size of the vertical and horizontal components of the velocity are of the same order, a clear violation of the small-slope approximation in the theory (the velocity of the filtrate as well as the slope of the filtrate front must be almost parallel to the surface of the impermeable boundary). A proper theoretical treatment of the filtrate within this region requires the use of scales different from those introduced in §3.2. This also implies that it is not justified, strictly speaking, using our predicted shape of the filtrate front within the region near $r = 0$ to satisfy the volume constraint, (43). (Note that the singular shape has the property that a vanishingly small volume of filtrate resides in the formation above the origin, despite the fact that the height of the interface approaches infinity.) However, by doing this, we are able to predict the location of the leading edge of the filtrate (the point furthest from the origin) based upon the outer solution alone. Thus, our justification for using (43) is based upon the degree of agreement between experiment and theory, in particular the ability of the theory to accurately predict the location of the filtrate's leading edge.

Another theoretical idealization of concern is the neglect of any transition zone between the regions fully saturated with the filtrate and with the formation fluid. The experiments show the existence of a diffuse transition region, an approximate location of its borders being indicated by the two curves identified using pattern recognition, refer to figure 16. Most likely this transition zone is a consequence of hydrodynamic dispersion, resulting in part from the heterogeneity of the sample, the thickness of the transition zone being too large to be solely a result of molecular diffusion. A direct consequence of ignoring the transition zone is the improper treatment of the filtrate front in the neighbourhood of the impermeable barrier, i.e. at the leading edge of the filtrate. When diffusive processes are present, the gradient in the concentration field, in this case salt, must be directed parallel to the impermeable surface. This implies that surfaces of constant salt concentration must terminate at right angles to the impermeable surface. Clearly, this is violated in the theoretical predictions of the shape of the interface, though it appears to be present in the experimentally determined shapes, refer to figures 21, 22 and 23. (The theory may be regarded as ignoring the dynamics of the fluids in an 'inner region' located in the immediate vicinity of the leading edge of the filtrate.) Despite this theoretical deficiency, the experiments show that adequate predictions are made for the location of the filtrate's leading edge. Also, in spite of the heterogeneity of the sample indicated in figure 5, theory based upon a homogeneous model gives rather good predictions.

The incorporation of this solution into the larger problem of filtrate invading a permeable bed from a wellbore, is addressed in Part 2.

The authors gratefully acknowledge David Wilkinson for bringing to our attention the importance of buoyancy segregation and for his useful technical dicussions, J. R. A. Pearson for identifying relevant existing literature and insightful comments, Brenda Schmidt for her assistance in setting up the experiments, and Andrew Reischer for aiding in the development of the pattern recognition algorithm.

REFERENCES

ALLEN, D. F., AUZERAIS, F. M., DUSSAN V., E. B., GOODE, P., RAMAKRISHNAN, T. S., SCHWARTZ, L., WILKINSON, D., FORDHAM, E., HAMMOND, P. & WILLIAMS, R. 1991 Invasion revisited. *Oilfield Rev.* **3** (3), 10.

AUZERAIS, F. M., DUSSAN V., E. B. & REISCHER, A. J. 1991 Computed tomography for the quantitative characterization of flow through a porous medium. *SPE 66th Annual Tech. Conf. Dallas, SPE* 22595.

BARENBLATT, G. I., ENTOV. V. M. & RYZHIK, V. M. 1990 *Theory of Fluid Flows Through Natural Rocks*. Kluwer.

DOLL, H. G. 1955 Filtrate invasion in highly permeable sands. *The Petrol Engr.*, January.

DUSSAN V., E. B. & AUZERAIS, F. M. 1993 Buoyancy-induced flow in porous media generated near a drilled oil well. Part 2. (In preparation).

ELLIS, D. V. 1987 *Well Logging for Earth Scientists*. Elsevier.

EVANS, R. D. 1955 *The Atomic Nucleus*. McGraw-Hill.

GRAY, G. R. & DARLEY, H. C. H. 1980 *Composition and Properties of Oil Well Drilling Fluids*, 4th Edn. Gulf.

WELLINGTON, S. L. & VINEGAR, H. J. 1987 X-ray computerized tomography. *J. Petrol. Technol.* **39**, 885–898.